SCIENCE CHINA
Physics, Mechanics & Astronomy

•Article•

April 2022 Vol. 65 No. 4: 247011
https://doi.org/10.1007/s11433-021-1834-4

Large magnetic entropy change in weberite-type oxides Gd_3MO_7 (M = Nb, Sb, and Ta)

Ziyu Yang[1], Shijun Qin[2], Xubin Ye[2], Zhehong Liu[2], Yujie Guo[1], Hongzhi Cui[1*], Jun-Yi Ge[4], Hui Li[5], Youwen Long[2,3*], and Yu-Jia Zeng[1*]

[1] *College of Civil and Transportation Engineering, College of Physics and Optoelectronic Engineering, Shenzhen University, Shenzhen 518060, China;*
[2] *Beijing National Laboratory for Condensed Matter Physics, Institute of Physics, Chinese Academy of Sciences, Beijing 100190, China;*
[3] *Songshan Lake Materials Laboratory, Dongguan 523808, China;*
[4] *Materials Genome Institute, Shanghai University, Shanghai 200444, China;*
[5] *College of Engineering Physics, Shenzhen Technology University, Shenzhen 518118, China*

Received October 13, 2021; accepted December 14, 2021; published online March 4, 2022

In the present work, the structure, magnetic properties, and cryogenic magnetocaloric effect of weberite-type oxides Gd_3MO_7 (M = Nb, Sb, and Ta) are reported through powder X-ray diffraction, bulk susceptibility, and heat capacity measurements, as well as scaling law analysis and a mean-field approach. A remarkably large isothermal magnetic entropy change of 354.0 mJ K^{-1} cm^{-3} is observed for Gd_3SbO_7 under an external field of 9 T at 2.0 K. The relative cooling power is estimated to be 618.9 J kg^{-1} (4.8 J cm^{-3}) for an applied field of 8.9 T, with the largest adiabatic temperature change being 22.4 K at 6.3 K. The magnetocaloric performance of these oxides is quite impressive when compared with the benchmark magnetic refrigerant, gadolinium gallium garnet ($Gd_3Ga_5O_{12}$, GGG). Therefore, Gd_3MO_7 (M = Nb, Sb, and Ta) are promising alternatives for cryogenic cooling techniques, especially for the magnetic liquefaction of helium.

magnetocaloric effect, antiferromagnetism, oxides, cryogenic, rare earths

PACS number(s): 47.55.nb, 47.20.Ky, 47.11.Fg

Citation: Z. Yang, S. Qin, X. Ye, Z. Liu, Y. Guo, H. Cui, J.-Y. Ge, H. Li, Y. Long, and Y.-J. Zeng, Large magnetic entropy change in weberite-type oxides Gd_3MO_7 (M = Nb, Sb, and Ta), Sci. China-Phys. Mech. Astron. **65**, 247011 (2022), https://doi.org/10.1007/s11433-021-1834-4

1 Introduction

Magnetic cooling is a field-driven refrigeration process associated with the magnetocaloric effect, which describes the change of magnetic entropy following the application of varied external fields. The overall efficiency of magnetic cooling can approach 60% of that of the theoretical Carnot cycle, making magnetocaloric materials a promising alternative to current refrigeration techniques [1-5]. A desired magnetocaloric material possesses a large isothermal magnetic entropy change, $-\Delta S_M$, and moderate heat capacity; thus, the heat generated during adiabatic magnetization-demagnetization cycles can result in a larger temperature change. In addition, technologically promising candidates should be able to cope with the demands of high mass density, easy processability, and have considerably robust resistance to chemical and mechanical erosion [3,6,7].

Intermetallic compounds containing lanthanides, metal-organic complexes, and rare earth ceramics are those typically proposed as efficient magnetic refrigerants [8]. In the

*Corresponding authors (Hongzhi Cui, email: h.z.cui@szu.edu.cn; Youwen Long, email: ywlong@iphy.ac.cn; Yu-Jia Zeng, email: yjzeng@szu.edu.cn)

cryogenic temperature range, Gd^{3+} containing ceramics are particularly appealing for their resistance to corrosive working substances, such as liquid hydrogen [2,4,9,10]. Gd^{3+} possesses a half-filled electron shell with the spherically symmetric ground state $^8S_{7/2}$, and a large spin-only magnetic moment can be expected for its relatively weak crystal electric field effects [6,11]. The total available molar magnetic entropy of one Gd^{3+} ion is $R\ln(2J + 1) = 17.3\ \mathrm{J\ K^{-1}\ mol^{-1}}$ (R is the gas constant), which is the highest entropy change value that can be reached for a single rare earth ion. Gadolinium gallium garnet ($Gd_3Ga_5O_{12}$, GGG), which was explored in the 1980s, has long been known to be the benchmark magnetocaloric material for cryogenic refrigeration, with a $-\Delta S_M$ of 300.2 mJ K^{-1} cm^{-3} under an applied field change of 9 T below 5 K [5]. Further elemental doping of GGG to improve its magnetocaloric performance has also been thoroughly investigated [12,13]. However, the $-\Delta S_M$ of GGG is far from satisfactory compared with the theoretical limit of 51.9 J K^{-1} mol^{-1} determined for materials containing three free Gd^{3+} ions. It is therefore appealing to explore new materials that express a more pronounced magnetocaloric effect, which is essential for the fabrication of future magnetic cooling devices with less energy consumption.

The ternary oxides Ln_3MO_7 are derived from polymorphic modifications of fluorite lattice $M_4^{+4}O_8$; Ln represents rare earth elements, and M represents pentavalent elements of Nb, Ta, Sb, Mo, Re, Ru, Ir, etc. These oxides show fascinating electrical, magnetic, and thermal properties due to their internal one-dimensional nature [14,15]. Among the Ln_3MO_7 family, the weberite-type structure forms when Ln^{3+} is in moderate ionic size and when M = Nb, Sb, and Ta. This structure crystallizes in an orthorhombic supercell with dimensions $a \approx 2a_{\mathrm{fluorite}}$ and $b \approx c \approx \sqrt{2}\,a_{\mathrm{fluorite}}$ [16]. The octahedrally coordinated [MO_6] polyhedrons form infinite zigzag chains along the orthorhombic c-axis and are well separated by rare earth chains of eight-coordinated [LnO_8] polyhedrons and seven coordinated [LnO_7] polyhedrons that occupy crystallographically inequivalent positions. This results in a relatively large density of magnetic ions and varied magnetic interactions. It is reasonable to infer that weberite-type oxides with Gd^{3+} occupying the rare earth sites may possess a large magnetocaloric effect, as evidenced by their large mass density and pronounced antiferromagnetic correlated ordering. Furthermore, the heat capacity of Gd_3MO_7 (M = Nb, Sb, and Ta) shows a moderate lattice contribution, indicating more efficient use of spin entropy changes, which lowers the internal heat load during magnetization-demagnetization cycles [15,17].

In the present work, we report on the structural, magnetic, and cryogenic magnetocaloric properties of weberite-type oxides Gd_3MO_7 (M = Nb, Sb, and Ta) through powder X-ray diffraction, bulk magnetization, and heat capacity measurements along with scaling analysis. A remarkably large isothermal magnetic entropy change, $-\Delta S_M(H, T)$, and relative cooling power (RCP) are identified such that Gd_3MO_7 oxides exhibit potential as working alternatives for cryogenic magnetic cooling, especially for the magnetic liquefaction of helium.

2 Materials and method

Polycrystalline Gd_3MO_7 (M = Nb, Sb, and Ta) powders were prepared using a traditional solid-state reaction process with Gd_2O_3 (5N, Adamas), Nb_2O_5 (4N, Adamas), Sb_2O_3 (3N, Sigma-Aldrich), and Ta_2O_5 (4N, Adamas) as starting materials. The Gd_2O_3 was dried at 1173 K for 20 h before use to remove adsorbed carbonate and water. Stoichiometric amounts of the raw oxides were mixed in an agate mortar, pressed into a φ-2-cm tablet under 2 tons of pressure, heated to 1673 K at a rate of 10 K h^{-1} for 12 h, and heated again to 1723 K for 12 h durations with re-grinding and re-pelleting in between.

The products were investigated using powder X-ray diffraction collected on a Rigaku Ultimate IV diffractometer equipped with Cu-Kα radiation at room temperature. Rietveld analysis was performed using the GSAS package with the EXPGUI interface [18]. The background and peak shapes were modeled by a Chebyshev polynomial of the first kind and a pseudo-Voigt function.

Heat capacity measurements were conducted using the thermal-relaxation method on pressed powder samples in a commercial physical property measurement system (PPMS-9, Quantum Design) with Apiezon N-grease under a temperature range of 1.9-40 K and constant external fields of 0, 2, and 8.9 T. Magnetic susceptibility and magnetization data were collected using another PPMS (PPMS®DynaCool™, Quantum Design) with an applied field of 10 mT in the 2-300 K temperature range. Isothermal magnetization curves were collected in a field range ≤9 T and temperature range of 2-25 K with a 1-K step after cooling in zero field.

3 Results and discussion

3.1 Crystallographic parameters

Figure 1(a) shows experimental powder X-ray diffraction patterns for Gd_3NbO_7 (GNO), Gd_3SbO_7 (GSO), and Gd_3TaO_7 (GTO) collected at room temperature, along with the theoretical fit using Bragg positions of the $C222_1$ crystallographic symmetry. The more symmetrical *Cmcm* space group is excluded due to the presence of weak $h0l$ reflections with even h and odd l, e.g., the (201) reflections at approximately 20.4° [17]. Rietveld refinement was carried out

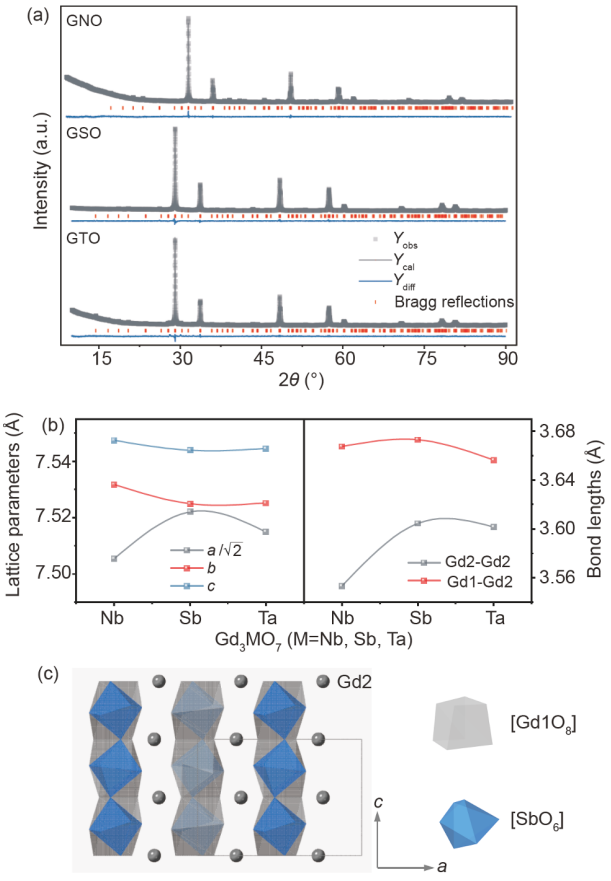

Figure 1 (Color online) (a) Room-temperature X-ray powder diffraction patterns and Rietveld analysis for Gd_3MO_7 (M = Nb, Sb, and Ta). (b) Lattice parameters and bond lengths of Gd_3MO_7 (M = Nb, Sb, and Ta). (c) Schematic crystal structures of Gd_3SbO_7; the gray solid line represents the unit cell, and [$Gd1O_8$] and [SbO_6] polyhedra are shown in gray and blue, respectively.

using the GSAS-EXPGUI package, and all of the observed diffraction peaks could be well indexed with the orthorhombic unit cell of $C222_1$ space symmetry (Y_3TaO_7-type) [18]. A goodness of fit, χ^2, of 1.581, 1.279, and 1.903 was achieved for GNO, GSO, and GTO, respectively.

Lattice parameters determined from the Rietveld analysis are listed in Table 1 and are consistent with previously reported values [15]. The variation of unit cell dimensions $a/\sqrt{2}$, b, c, and the Gd–Gd bond lengths against the M sites are plotted in Figure 1(b). The lattice dimension $a/\sqrt{2}$ of GNO is slightly smaller than GTO, while b and c dimensions are larger. However, the six-coordinated Nb^{5+} and Ta^{5+} are almost in the same Shannon ionic radius (0.64 Å) [19]. GSO shows the largest rare earth bond lengths: 3.6045(53) and 3.6731(59) Å for the nearest and the next nearest Gd–Gd lengths, respectively.

Two kinds of one-dimensional chains exist in the weberite-type lattice, as in the GSO, of which six-coordinated antimony atoms and eight-coordinated gadolinium atoms form zig-zag chains running parallel to the <001> direction, as depicted in Figure 1(c). In the distorted [SbO_6] polyhedron, two of the equatorial Sb–O bonds are 2.256(31) Å, while the left two are slightly shorter (2.050(30) Å). The [SbO_6] polyhedra are connected by sharing apical oxygens [O5] and tilt along the c-axis, while rare earth chains are formed by edge-sharing [$Gd1O_8$] pseudocubes. The left Gd^{3+} ions, denoted as Gd2, occupy a crystallographically inequivalent position, which is seven-coordinated by oxygen atoms and exists between the [SbO_6] and [$Gd1O_8$] slabs (Figure 1(c)).

3.2 Magnetic susceptibility

Figure 2(a) depicts the zero-field-cooled magnetic susceptibility of Gd_3MO_7 (M = Nb, Sb, and Ta) measured under an applied field of 10 mT. The results show no indication of long-range magnetic order for GNO or GTO but an antiferromagnetic ordering transition for GSO, as evidenced by the sharp peak cusp in the dc susceptibility curve. For $T >$ 7 K, all of the dc susceptibility curves can be well described in terms of the Curie-Weiss law, giving an antiferromagnetic Weiss temperature, θ_{CW}, of −7.2, −13.5, and −9.1 K for GNO, GSO, and GTO, respectively, as shown in the Figure 2(a) inset. A negative Weiss temperature indicates that the dominating interactions are antiferromagnetically correlated [20]. The calculated effective magnetic moments are 7.95 μ_B, 8.04 μ_B, and 7.95 μ_B for GNO, GSO, and GTO, respectively, and are broadly consistent with values expected for spin-only Gd^{3+} according to Russel-Saunders coupling ($^8S_{7/2}$ term).

Notably, the long-range ordering transition temperature is less than 1/4 of the θ_{CW} for all three weberites, indicating a possibly inherent frustration or competitive interactions of

Table 1 Crystallographic data and Rietveld analysis results for Gd_3MO_7 (M = Nb, Sb, and Ta)[a)]

Formula	M_w (g/mol)	Crystal system	S.G.	Unit cell dimensions (Å)	V_{cell} (Å³)	Asymmetric unit	ρ_{cal} (g/cm³)	χ^2	R indices[a)]
Gd_3NbO_7	676.65	orthorhombic	$C222_1$	a = 10.6143(5) b = 7.5318(4) c = 7.5475(4)	603.383	8 sites	7.4505	1.581	R_{wp} = 2.30%, R_p = 1.81%
Gd_3SbO_7	705.51	orthorhombic	$C222_1$	a = 10.6378(8) b = 7.5249(5) c = 7.5439(5)	603.877	8 sites	7.7622	1.279	R_{wp} = 4.14%, R_p = 3.16%
Gd_3TaO_7	764.69	orthorhombic	$C222_1$	a = 10.6278(9) b = 7.5251(6) c = 7.5445(6)	603.373	8 sites	8.4193	1.903	R_{wp} = 2.76%, R_p = 2.09%

a) $R_{wp} = \left[\sum_i w_i\left(y_i - f_i(x)\right)^2 / \sum_i w_i y_i^2\right]^{1/2}$, $R_p = \sum\left|I_k(o) - I_k(c)\right| / \sum I_k(o)$.

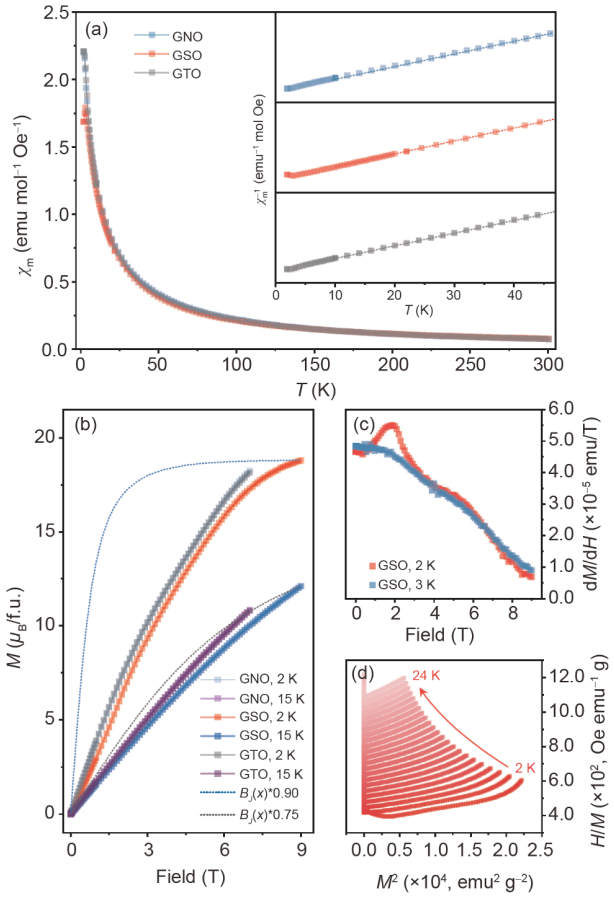

Figure 2 (Color online) Magnetic characterization of Gd_3MO_7 (M = Nb, Sb, and Ta). (a) DC magnetic susceptibility collected under an applied field of 100 Oe. Inset: Curie-Weiss fitting of the inverse magnetic susceptibility, χ_m^{-1}. (b) Field variance of the isothermal magnetization curves at 2 and 15 K. Theoretical curves of the Brillouin function corresponding to free three-ion systems with $J = S = 7/2$ are shown by the dashed lines. (c) Derivative, dM/dH, of the magnetization curves for GSO at 2 and 3 K. (d) Standard Arrott isotherms showing the Banerjee criterion for GSO.

the Gd^{3+} spin network. By calculating $f = \theta_{CW}/T_N$, $f = 5.6$ is deduced for GSO, which corresponds to a moderately frustrated magnetic system [21]. The frustration possibly arises from geometric configurations of Gd^{3+}, as the $C222_1$ crystallographic symmetry can be viewed as an intricate three-dimensional pyrochlore lattice, which is composed of dominating triangular plaquettes and square plaquettes for two-thirds of the Gd^{3+} ions [22]. The remaining rare earth sites form an interlocked second pyrochlore lattice, in direct analogy with a typical pyrochlore compound $Ln_2Ti_2O_7$ (Ln = rare earth) [23].

The splitting of the (2J+1)-fold ground state primarily arises from the anisotropic orbital angular momentum. Thus, crystal electric field effects are expected to be relatively feeble in the Gd^{3+} ions spin network. The seven electrons in Gd^{3+} form a half-filled f shell with quenched angular momentum, generating an isotropic spin-only $S = J = 7/2$ [11]. Therefore, the comprehensive interactions can be realistically interpreted via a standard mean-field (M.F.) estimate, parameterized by the strength of the nearest-neighbor interaction, J_{nn}, and the dipolar interaction, D_{nn} [11,13].

Table 2 shows the changes in the approximately calculated exchange J_{nn} and the D_{nn}, and their ratio D_{nn}/J_{nn}. D_{nn} is almost the same magnitude for all Gd_3MO_7 (M = Nb, Sb, and Ta), while the J_{nn} of GSO (−2.45 K) is obviously larger than the other two compounds (−1.53 and −1.73 K for GNO and GTO, respectively), indicating a stronger antiferromagnetic interaction [13]. The changes in exchange J_{nn} are further revealed by the suppression of both the magnetic susceptibility, χ_m, and the isothermal magnetization, M, under wide temperature (2 to 24 K) and field ranges (0 to 7 T). This indicates that the interplay between J_{nn} and D_{nn} exerts intensively on the magnetic ground state, as depicted in Figure 2(b).

The isothermal magnetization curves measured at 2 and 15 K are shown in Figure 2(b), as well as the theoretical description of the M-H dependence of the non-interacting three-ion system with $J = S = 7/2$ using the Brillouin function [11]. At the highest experimental field of 9 T, the magnetic moment per Gd^{3+} for GSO reaches approximately 90% and 75% of that of the saturation moment for theoretical interpretations at 2 and 15 K, respectively. The magnetization curves follow a linear behavior up to an applied field of around 3 T; no saturation effect sets in, even at the highest experimental field H = 9 T. The field dependence of isothermal magnetization curves is in stark deviation from the Brillouin description of non-interacting paramagnetic ions, indicating the presence of effective internal fields generated by the interactions of dipolar and the exchange nature. This is in agreement with the susceptibility measurement.

Above T_N, dM/dH of GSO exhibits monotonic, continuous behavior, while a broad maximum is discernible under temperatures below T_N. This characterizes a possible field-induced transition, as shown in Figure 2(c). Standard Arrott isotherms for GSO are plotted in Figure 2(d). A negative slope is observed in the field-induced transition region (applied field $H < 3$ T, $T = 2$ K), which is typically attributed to a first-order transition, while the antiferromagnetic-paramagnetic phase transition is second order in nature, according to the Banerjee criterion [24].

3.3 Heat capacity

Temperature and field variance of heat capacity normalized

Table 2 Bulk magnetic properties, dipolar interaction (D_{nn}), and the nearest-neighbor exchange interaction (J_{nn}) for Gd_3MO_7 (M = Nb, Sb, and Ta)

Compounds	μ_{eff} (μ_B)	θ_{CW} (K)	D_{nn} (K)	J_{nn} (K)	D_{nn}/J_{nn}
GNO	7.95	−7.2	−0.88	−1.53	0.58
GSO	8.04	−13.5	−0.86	−2.45	0.35
GTO	7.95	−9.1	−0.84	−1.73	0.49

to the gas constant for GSO, C_p/R, shows long-range antiferromagnetic ordering at 2.4 K. This was identified by dc susceptibility measurements (Figure 3(a)). The ordering transition shifts to a lower temperature at 2 T and manifests a broad feature at 8.9 T, denoting a field-induced transition as characterized by Arrott isotherms (Figure 2(d)). The lattice contribution of phonon modes is estimated by fitting the experimental data at 0 T in terms of the Debye model with a polynomial expression: $C_L = \alpha RT^3 + BT^5 + CT^7$. This expression yields a constant of $\alpha = 1.1 \times 10^{-4}$, which is comparable to that of the commercial cryo-coolant $Gd_3Ga_5O_{12}$ (GGG, $\alpha = 3 \times 10^{-5}$) [5]. A low lattice phonon mode will ultimately favor the magnetocaloric effect as a minor internal heat load is produced during magnetization-demagnetization cycles.

Theoretically, the total entropy can be calculated by integrating the thermodynamic relation:

$$S_T(H,T) = \int_0^{T_{\rm fin}} \frac{Cp\mathrm{d}T}{T}, \tag{1}$$

in which a proper extrapolation of the heat capacity data to $T \to 0$ is needed. However, this is not always feasible due to pronounced peak anomalies, especially those under low applied fields. In the present case, the highest experimental temperature, $T = 40$ K, is almost 16 times higher than that of the antiferromagnetic ordering temperature; thus, a numerical estimation of magnetic entropy for the paramagnetic state using the M.F. model is applicable. This estimation is given by

$$S_{\rm M}(H,T) = N_A k_{\rm B}\left[\ln\frac{\sinh\left[\left(1+\frac{1}{2S}\right)x\right]}{\sinh\left(\frac{x}{2S}\right)} - xB_J(x)\right], \tag{2}$$

where $B_J(x)$ represents the Brillouin function with spin S and $x = Sg\mu_{\rm B}\mu_0 H/k_{\rm B}T$.

When $x << 1$, the first term of eq. (2) can be approximated to $\ln(2S+1)$ and $xB_J(x) \approx CH^2/2T^2$, where C represents the Curie constant. For a simple two-sublattice antiferromagnet, when $T >> T_N$, the above expression can be approximated via replacing H by a mean-field $H_{MF} = HT/(T+\Theta_{MF})$ [9]. This gives

$$S_{\rm M}(H,T) = N_A k_{\rm B}\ln(2S+1) - \frac{CH^2}{2(T+\Theta_{MF})^2}. \tag{3}$$

By adjusting the mean-field value, $\Theta_{MF} = 4.3$ K is deduced to get a good fit of $S_T(H,T)$ using eq. (2) for $H = 8.9$ T at the temperature range of ~5-10 K, where the phonon contribu-

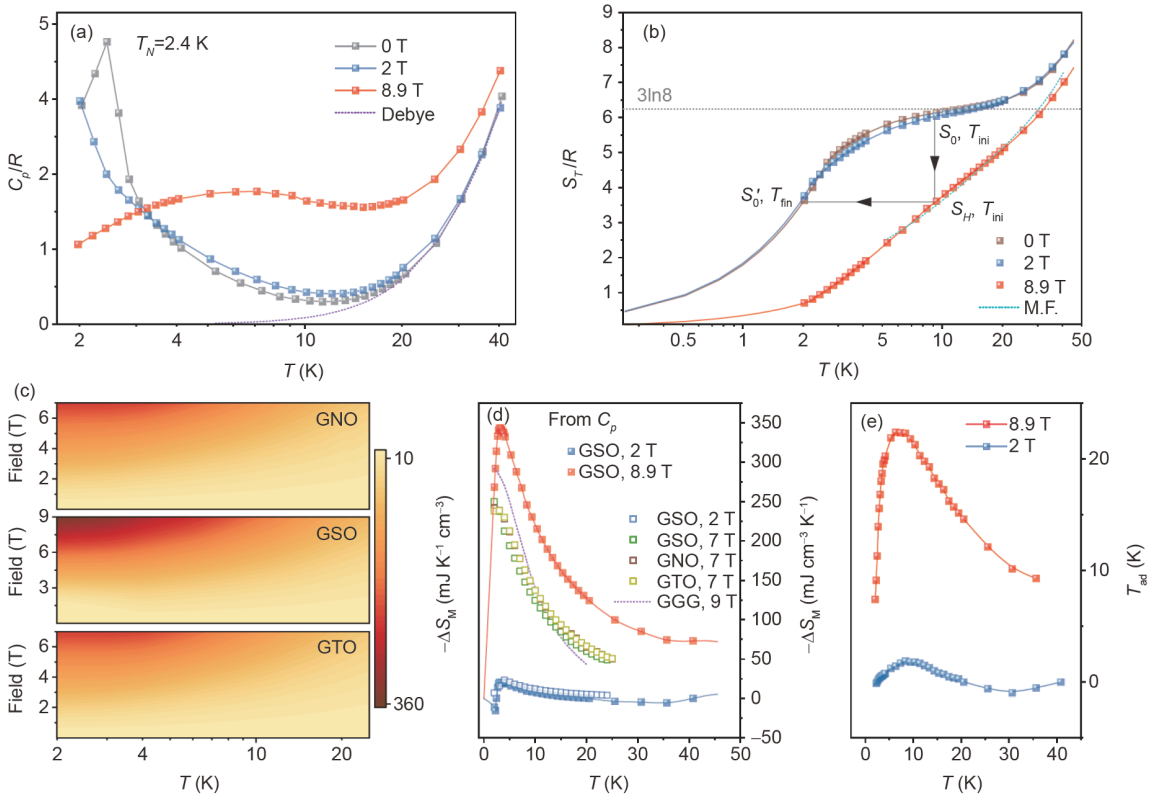

Figure 3 (Color online) (a) Logarithmic representation of the temperature variance of heat capacity normalized to the gas constant, C_p/R, collected for constant fields of 0, 2, and 8.9 T for GSO. The dashed line corresponds to the lattice contribution estimated by the Debye model. (b) Experimentally determined entropy, S_T/R, deduced by the integration of C_p/T with a dashed line representing the mean-field approximation of eq. (2). Arrows depict the calculation of the isothermal magnetic entropy change, $-\Delta S_{\rm M}(H,T)$, by $S_0 - S_H$ and the adiabatic temperature change, $T_{\rm ad}$, by $T_{\rm ini} - T_{\rm fin}$. (c) $-\Delta S_{\rm M}(H,T)$ in contour plots as a variation of applied field and temperature for GNO, GSO, and GTO. (d) Temperature variance of $-\Delta S_{\rm M}(H,T)$ obtained from the Maxwell relation (open marks) and datasets from the integration of heat capacity (close marks) for selected applied fields of 2, 7, 8.9, and 9 T. The dashed line corresponds to the magnetic entropy change of GGG at 9 T. (e) Adiabatic temperature change, $T_{\rm ad}$, under external fields of 2 and 8.9 T.

tion is negligible, as depicted in Figure 3(b). Then, eq. (3) is further used to determine the difference of magnetic entropy for external fields of 0 and 2 T at the highest experimental temperature, $T = 40$ K. The obtained entropy diagram, S_T-T, under fields of 0, 2, and 8.9 T is depicted in Figure 3(b). Notably, the magnetic entropy under a field of 0 T approaches $3R\ln 8$ at ~10 K, where the lattice contributions are negligibly small. This indicates complete long-range antiferromagnetic ordering among the interacting Gd^{3+} spin network.

3.4 Magnetocaloric effect

The thermal variance of the magnetic entropy change curves, $-\Delta S_M(H,T)$, for different constant fields can be calculated from half of the theoretical Carnot cycle,

$$\Delta S_M(\Delta H, T) = S(H, T) - S(0, T), \tag{4}$$

as depicted in Figure 3(b), where the heat released to a warm source is $Q = T_{ini}(S_H - S_0)$. During the adiabatic demagnetization process, the temperature is then reduced to T_{fin} at the isentropic point, (S_0', T_{fin}), giving the adiabatic temperature change, $T_{ad} = T_{ini} - T_{fin}$.

Equivalent datasets of $-\Delta S_M(H,T)$ can also be indirectly evaluated from the isothermal process of magnetization according to the Maxwell thermodynamic relation,

$$\left(\frac{\partial S}{\partial H}\right)_T = \left(\frac{\partial M}{\partial T}\right)_H \Rightarrow \Delta S_M(H, T) = \int_0^H \left(\frac{\partial M}{\partial T}\right)_H \mathrm{d}H, \tag{5}$$

of which, for an isobaric process, the integral is numerically approximated by the sum

$$\Delta S_M(H, T) = \sum \frac{(M_{j+1} - M_j)_H}{T_{j+1} - T_j}(H_{i+1} - H_i), \tag{6}$$

where $M_{j+1} - M_j$ represents the incremental changes in magnetization values under a temperature increment of $T_{j+1} - T_j$ [3,25]. The stepwise increase of magnetic field $H_{i+1} - H_i$ generally starts from $H_1 = 0$.

The two corresponding sets of magnetic entropy change values deduced from eqs. (4) and (6) superimpose onto each other rather nicely, as depicted in Figure 3(d). Further contour plots as a function of T and H are depicted in Figure 3(c) and are quantified from the experimental magnetic isotherms recorded in the range of 2-25 K for GNO and GTO, and 2-24 K for GSO, respectively.

Among the three weberites, $-\Delta S_M(H,T)$ shows a monotonous decrease with increasing temperature. The maximum values of $-\Delta S_M(H,T)$ are observed for GSO around T_N and are 33.0 and 45.6 J K^{-1} kg^{-1} for an applied magnetic field variation of 0-7 T and 0-9 T, respectively. The corresponding entropy changes of GNO and GTO are marginally smaller than GSO, 32.4 and 28.3 J K^{-1} kg^{-1} under a field of 7 T, due to decreased magnetic phase transition temperatures. The volumetric unit, mJ K^{-1} cm^{-3}, taken as the product of the density, ρ, and the value of $-\Delta S_M(H,T)$ in gravimetric units, are better references for assessing the implementation of magnetocaloric materials in an engineering apparatus [4,6]. Values of 256.2 and 354.0 mJ K^{-1} cm^{-3} are deduced for GSO under an applied field change of 0-7 T and 0-9 T at 2 K, respectively, which are significantly large.

The magnetocaloric performance of GSO is quite impressive when compared to GGG (42.4 J K^{-1} kg^{-1}, 300.2 mJ K^{-1} cm^{-3} at 9 T) in both gravimetric and volumetric units. GGG is the benchmark magnetic refrigerant at the 1 K < T < 5 K regime [5]. Notably, $-\Delta S_M(H,T)$ is superior for the entire temperature range of ~2-20 K, as depicted in Figure 3(d). Furthermore, the maximum adiabatic temperature change, T_{ad}, is estimated to be 22.4 K for an applied field of 8.9 T, which is comparable to GGG (20 K for a field change of 9.4 → 0.7 T), as shown in Figure 3(e) [5]. The magnetocaloric performance of Gd_3MO_7 (M = Nb, Sb, and Ta) is comparable to a series of rare-earth-based magnetocaloric materials reported in recent literature, such as Gd_2ZnMnO_6, Gd_2FeAlO_6, and Sr_2GdNbO_6 [26]. This further supports the potential application of Gd_3MO_7 (M = Nb, Sb, and Ta) in cryogenic magnetic cooling, as summarized in Table 3 [26-37].

The superior magnetic entropy change values are likely attributed to the combination of large effective moments of Gd^{3+} spins and small magnetic anisotropy, as well as efficient use of spinentropy for the heat transfer process, as evidenced by their small phonon contributions to the heat capacity in Gd_3MO_7. Furthermore, the corner-sharing [SbO_6] polyhedra and edge-sharing [$Gd1O_8$] polyhedra form dense one-dimensional slabs, resulting in relatively large mass densities, ρ = 7.4505, ρ = 7.7622, and ρ = 8.4193 g cm^{-3} for GNO, GSO, and GTO, respectively. Consequently, the magnetocaloric performance of these materials is significantly enhanced.

To assess potential applications of Gd_3MO_7, another widely used parameter, refrigerant capacity (*RC*), is adopted. The *RC* is characterized by the magnitude of heat transfer between the cold T_{cold} and hot T_{hot} reservoirs,

$$RC = \int_{T_{cold}}^{T_{hot}} -\Delta S_M(H, T)\mathrm{d}T. \tag{7}$$

This is generally accomplished by estimating the RCP, which is defined as the product of the maximum of magnetic entropy change values and the corresponding full width at half maximum of the $-\Delta S_M(H,T)$ curve [1,3,4,6]. The pronounced maximum of RCP for GSO is 618.9 J kg^{-1} (4.8 J cm^{-3}) under an external field change of 8.9 T, which is exceptionally large among rare earth ceramics.

3.5 Scaling analysis

Scaling laws characterizing the applied field variance of magnetocaloric responses, i.e., the RCP, and the peak value

of magnetic entropy change, ΔS_{max}, at the corresponding magnetic field variation, are expressed by RCP $\propto H^{1+1/\delta}$ and $\Delta S_{max} \propto H^{n}$, respectively [25,38]. The critical exponents, δ and n, which parameterize the power law, are thus extracted as depicted in Figure 4(a) and (b).

According to the theoretical predictions, scaling exerts

Table 3 Representative magnetocaloric materials and their characteristics in the cryogenic temperature range, $T < 5$ K

Formula	$-\Delta S_M$ (mJ K^{-1} cm^{-3})	T (K)	ΔH (T)	Ref.
Gd_3SbO_7	354.0	2	9	this work
Gd_3NbO_7	241.4	2	7	this work
Gd_3TaO_7	238.3	2	7	this work
$Gd_3Ga_5O_{12}$ (GGG)	300.2	2	9	[5]
$GdAlO_3$	317	2	9	[26]
$GdCrO_3$	303	4	9	[27]
$[Gd(HCOO)(bdc)]_n$	125	2	9	[28]
Gd_3BWO_9	454	2.4	9	[10]
Gd_2ZnTiO_6	398.5	3.1	9	[7]
$[Gd(C_4O_4)(OH)(H_2O)_4]_n$	112.7	3	9	[29]
$K_2Gd(BH_4)_5$	59.8	5	9	[30]
$EuHo_2O_4$	267	2	8	[31]
$EuDy_2O_4$	224	2	8	[31]
$Gd_2Cu(SO_{4)2}(OH)_4$	212.8	4	8	[32]
$K_3Li_3Gd_7(BO_3)_9$	277.2	2	7	[33]
$Gd(OH)SO_4$	276	2	7	[34]
Gd_2NiMnO_6	268	4	7	[35]
$Gd(HCOO)_3$	215.7	2	7	[36]
$[Gd_4(SO_4)_4(\mu_3\text{-}OH)_4(H_2O)]_n$	198.9	2	7	[37]

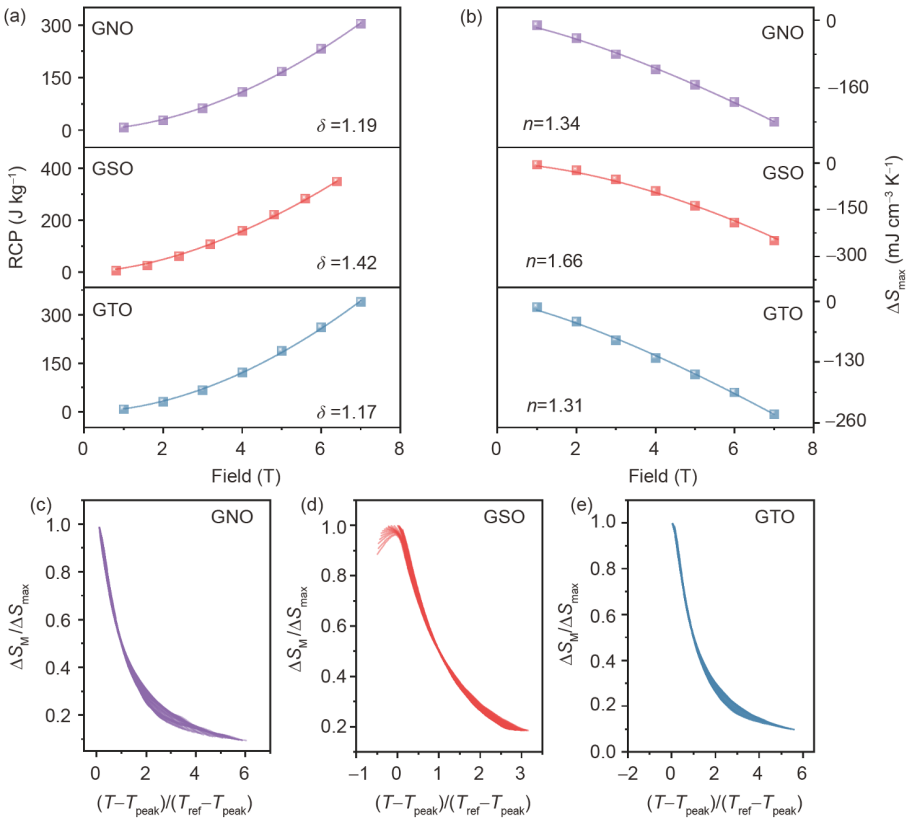

Figure 4 (Color online) (a), (b) Field variance (< 7 T) of the relative cooling power, RCP, and the peak magnetic entropy change, ΔS_{max}. Solid lines represent fits of the experimental data. (c)-(e) Single master curve behavior showing the collapse of $-\Delta S_M(H,T)$ curves at varied fields.

near a second-order phase transition, which can be demonstrated by the universality of the $-\Delta S_M(H,T)$ curves [4,25,38]. The phenomenological universal curve is processed via assessing the equivalent points of temperature and $-\Delta S_M(H,T)$, i.e., by normalizing the magnetic entropy change curve to the corresponding maximum via $\Delta S_M / \Delta S_{max}$ and rescaling the temperature axis to $(T - T_{peak})/(T_{ref} - T_{peak})$, where T_{peak} represents the temperature of peak entropy change and T_{ref} is the reference temperature corresponding to the half maximum of the peak magnetic entropy change, $\Delta S_M(H,T_{ref}) = 1/2\Delta S_{max}$, measured at different applied field changes.

The constructed curves are depicted in Figure 4(c)-(e), which express a pronounced single master curve behavior, i.e., the set of $-\Delta S_M(H,T)$ curves measured under different applied magnetic field changes collapse onto a universal curve, strongly supporting the second-order phase transition character for Gd_3MO_7 (M = Nb, Sb, and Ta).

4 Conclusions

In summary, we have prepared a series of weberite-type compounds, Gd_3MO_7 (M = Nb, Sb, and Ta), through a traditional solid-state reaction and investigated their crystallographic structure and bulk magnetic properties. The magnetocaloric effects are experimentally determined by an indirect approach, yielding a significantly large magnetic entropy change for GSO of 354.0 mJ K^{-1} cm^{-3} under an applied field of 9 T at 2 K. The RCP is estimated to be 618.9 J kg^{-1} (4.8 J cm^{-3}) for a field of 8.9 T, with the largest adiabatic temperature change of 22.4 K at 6.3 K. The superior magnetocaloric performance makes Gd_3MO_7 weberite-type compounds strong candidates as magnetic refrigerants at liquid helium temperature and competitive with the benchmark cryogenic magnetocaloric material, GGG.

This work was supported by the Science, Technology and Innovation Commission of Shenzhen Municipality (Grant Nos. JCYJ20190808152-217447, JCYJ20180305125212075, JCYJ20180507182246321, and JCYJ20210324095611032), the National Natural Science Foundation of China (Grant Nos. 51925804, 11904236, 11934017, and 11921004), the Beijing Natural Science Foundation (Grant No. Z200007), the National Key R&D Program of China (Grant Nos. 2018YFE0103200, and 2018YFA0305700), and the Chinese Academy of Sciences (Grant No. XDB33000000). Hui Li is also thankful for the support from the Young Innovative Talents Project for Regular Universities in Guangdong Province (Grant No. 2018KQNCX396).

1 M. Balli, S. Jandl, P. Fournier, and A. Kedous-Lebouc, Appl. Phys. Rev. **4**, 021305 (2017).
2 J. Lyubina, J. Phys. D-Appl. Phys. **50**, 053002 (2017).
3 N. A. de Oliveira, and P. J. von Ranke, Phys. Rep. **489**, 89 (2010).
4 V. Franco, J. S. Blázquez, J. J. Ipus, J. Y. Law, L. M. Moreno-Ramírez, and A. Conde, Prog. Mater. Sci. **93**, 112 (2018); H. F. Kirby, D. D. Belyea, J. T. Willman, and C. W. Miller, J. Vacuum Sci. Tech. A-Vacuum Surfs Films **31**, 031506 (2013).
5 J. A. Barclay, and W. A. Steyert, Cryogenics **22**, 73 (1982); P. Mukherjee, A. C. Sackville Hamilton, H. F. J. Glass, and S. E. Dutton, J. Phys.-Condens. Matter **29**, 405808 (2017), arXiv: 1707.06730.
6 A. Kitanovski, J. Tušek, U. Tomc, U. Plaznik, M. Ožbolt, and A. Poredoš, in *Magnetocaloric Energy Conversion From Theory to Applications*, edited by A. Kitanovski, J. Tušek, U. Tomc, U. Plaznik, M. Ožbolt, and A. Poredoš (Springer, Heidelberg, 2015), pp. 1-21.
7 Z. Yang, J. Y. Ge, S. Ruan, H. Cui, and Y. J. Zeng, J. Mater. Chem. C **9**, 6754 (2021).
8 L. S. Chen, J. Z. Zhang, L. Wen, P. Yu, and L. Xia, Sci. China-Phys. Mech. Astron. **61**, 056121 (2018); F. X. Liu, H. Zhang, H. Zhou, D. Y. Cong, R. J. Huang, L. C. Wang, and Y. Long, Sci. China-Phys. Mech. Astron. **63**, 277511 (2020); Z. Ma, X. Dong, Z. Zhang, and L. Li, J. Mater. Sci. Tech. **92**, 138 (2021); Y. Zhang, J. Zhu, S. Li, J. Wang, and Z. Ren, J. Mater. Sci. Tech. **102**, 66 (2022); H. Xiang, Y. Xing, F. Dai, H. Wang, L. Su, L. Miao, G. Zhang, Y. Wang, X. Qi, L. Yao, H. Wang, B. Zhao, J. Li, and Y. Zhou, J. Adv. Ceram. **10**, 385 (2021).
9 E. Palacios, M. Evangelisti, R. Sáez-Puche, A. J. Dos Santos-García, F. Fernández-Martínez, C. Cascales, M. Castro, R. Burriel, O. Fabelo, and J. A. Rodríguez-Velamazán, Phys. Rev. B **97**, 214401 (2018); E. Palacios, J. A. Rodríguez-Velamazán, M. Evangelisti, G. J. McIntyre, G. Lorusso, D. Visser, L. J. de Jongh, and L. A. Boatner, Phys. Rev. B **90**, 214423 (2014).
10 Z. Yang, H. Zhang, M. Bai, W. Li, S. Huang, S. Ruan, and Y. J. Zeng, J. Mater. Chem. C **8**, 11866 (2020).
11 J. M. D. Coey, in *Magnetism and Magnetic Materials*, edited by J. M. D. Coey (Cambridge University Press, Cambridge, 2001), pp. 97-127.
12 N. K. C. Muniraju, R. Baral, Y. Tian, R. Li, N. Poudel, K. Gofryk, N. Barišić, B. Kiefer, J. H. Ross Jr., and H. S. Nair, Inorg. Chem. **59**, 15144 (2020).
13 A. C. S. Hamilton, G. I. Lampronti, S. E. Rowley, and S. E. Dutton, J. Phys.-Condens. Matter **26**, 116001 (2014).
14 Y. Hinatsu, and Y. Doi, J. Solid State Chem. **198**, 176 (2013); Y. Hinatsu, Y. Doi, and M. Wakeshima, J. Solid State Chem. **262**, 224 (2018); M. Inabayashi, Y. Doi, M. Wakeshima, and Y. Hinatsu, J. Solid State Chem. **250**, 100 (2017); M. Inabayashi, Y. Doi, M. Wakeshima, and Y. Hinatsu, J. Ceram. Soc. Jpn. **126**, 920 (2018).
15 Y. Hinatsu, H. Ebisawa, and Y. Doi, J. Solid State Chem. **182**, 1694 (2009).
16 M. Wakeshima, H. Nishimine, and Y. Hinatsu, J. Phys.-Condens. Matter **16**, 4103 (2004).
17 M. Wakeshima, and Y. Hinatsu, J. Solid State Chem. **183**, 2681 (2010).
18 H. M. Rietveld, J. Appl. Crystlogr. **2**, 65 (1969).
19 R. D. Shannon, and C. T. Prewitt, Acta Crystallogr. B Struct. Crystallogr. Cryst. Chem. **26**, 1046 (1970).
20 Z. Yang, H. Zhang, J. Xu, R. Ma, T. Sasaki, Y. J. Zeng, S. Ruan, and Y. Hou, Natl. Sci. Rev. **7**, 841 (2020).
21 P. Mukherjee, and S. E. Dutton, Adv. Funct. Mater. **27**, 1701950 (2017).
22 T. Fennell, S. T. Bramwell, and M. A. Green, Can. J. Phys. **79**, 1415 (2001).
23 O. A. Petrenko, M. R. Lees, G. Balakrishnan, V. N. Glazkov, and S. S. Sosin, Phys. Rev. B **85**, 180412 (2012), arXiv: 1203.6326.
24 S. Bustingorry, F. Pomiro, G. Aurelio, and J. Curiale, Phys. Rev. B **93**, 224429 (2016); B. K. Banerjee, Phys. Lett. **12**, 16 (1964).
25 A. Zeleňáková, P. Hrubovčák, O. Kapusta, V. Zeleňák, and V. Franco, Appl. Phys. Lett. **109**, 122412 (2016).
26 S. Mahana, U. Manju, and D. Topwal, J. Phys. D-Appl. Phys. **50**, 035002 (2016); P. Xu, Z. Ma, P. Wang, H. Wang, and L. Li, Mater. Today Phys. **20**, 100470 (2021); B. Wu, Y. Zhang, D. Guo, J. Wang, and Z. Ren, Ceram. Int. **47**, 6290 (2021); L. Li, P. Xu, S. Ye, Y. Li, G. Liu, D. Huo, and M. Yan, Acta Mater. **194**, 354 (2020).
27 S. Mahana, U. Manju, and D. Topwal, J. Phys. D-Appl. Phys. **51**, 305002 (2018).
28 R. Sibille, T. Mazet, B. Malaman, and M. François, Chem. Eur. J. **18**,

12970 (2012).
29 S. Biswas, A. Adhikary, S. Goswami, and S. Konar, Dalton Trans. **42**, 13331 (2013).
30 P. Schouwink, E. Didelot, Y. S. Lee, T. Mazet, and R. Černý, J. Alloys Compd. **664**, 378 (2016).
31 A. Midya, N. Khan, D. Bhoi, and P. Mandal, Appl. Phys. Lett. **101**, 132415 (2012), arXiv: 1209.2513.
32 Y. Tang, W. Guo, S. Zhang, M. Yang, H. Xiang, and Z. He, Dalton Trans. **44**, 17026 (2015).
33 M. Xia, S. Shen, J. Lu, Y. Sun, and R. Li, Chem. Eur. J. **24**, 3147 (2018).
34 Y. Han, S. D. Han, J. Pan, Y. J. Ma, and G. M. Wang, Mater. Chem. Front. **2**, 2327 (2018).
35 J. K. Murthy, K. D. Chandrasekhar, S. Mahana, D. Topwal, and A. Venimadhav, J. Phys. D-Appl. Phys. **48**, 355001 (2015), arXiv: 1508.00087.
36 G. Lorusso, J. W. Sharples, E. Palacios, O. Roubeau, E. K. Brechin, R. Sessoli, A. Rossin, F. Tuna, E. J. L. McInnes, D. Collison, and M. Evangelisti, Adv. Mater. **25**, 4653 (2013).
37 S. D. Han, X. H. Miao, S. J. Liu, and X. H. Bu, Inorg. Chem. Front. **1**, 549 (2014).
38 V. Franco, and A. Conde, Int. J. Refrigerat. **33**, 465 (2010); V. Franco, A. Conde, V. Provenzano, and R. D. Shull, J. Magn. Magn. Mater. **322**, 218 (2010).